Talanta 261 (2023) 124655

Contents lists available at ScienceDirect

Talanta

journal homepage: www.elsevier.com/locate/talanta

Using staining as reference for spectral imaging: Its application for the development of an analytical method to predict the presence of bacterial biofilms

Nazan Altun [a,b,c,d], Martín F. Hervello [a], Felipe Lombó [b,c,d,*], Pelayo González [a,**]

[a] ASINCAR Agrifood Technology Center, Spain
[b] Research Unit "Biotechnology in Nutraceuticals and Bioactive Compounds-BIONUC", Departamento de Biología Funcional, Área de Microbiología, Universidad de Oviedo, Oviedo, Spain
[c] Instituto Universitario de Oncología del Principado de Asturias (IUOPA), Oviedo, Spain
[d] Instituto de Investigación Sanitaria del Principado de Asturias (ISPA), Oviedo, Spain

ARTICLE INFO

Handling Editor: Kin-ichi Tsunoda

Keywords:
Spectral imaging
Hyperspectral
Image treatment
Staining
Biofilm
Machine learning
Neural networks

ABSTRACT

At present, although spectral imaging is known to have a great potential to provide a massive amount of valuable information, the lack of reference methods remains as one of the bottlenecks to access the full capacity of this technique. This work aims to present a staining-based reference method with digital image treatment for spectral imaging, in order to propose a fast, efficient, contactless and non-invasive analytical method to predict the presence of biofilms. Spectral images of *Pseudomonas aeruginosa* biofilms formed on high density polyethylene coupons were acquired in visible and near infrared (vis-NIR) range between 400 and 1000 nm. Crystal violet staining served as a biofilm indicator, allowing the bacterial cells and the extracellular matrix to be marked on the coupon. Treated digital images of the stained biofilms were used as a reference. The size and pixels of the hyperspectral and digital images were scaled and matched to each other. Intensity color thresholds were used to differentiate the pixels associate to areas containing biofilms from those ones placed in biofilm-free areas. The model facultative Gram-negative bacterium, *P. aeruginosa*, which can form highly irregularly shaped and heterogeneous biofilm structures, was used to enhance the strength of the method, due to its inherent difficulties. The results showed that the areas with high and low intensities were modeled with good performance, but the moderate intensity areas (with potentially weak or nascent biofilms) were quite challenging. Image processing and artificial neural networks (ANN) methods were performed to overcome the issues resulted from biofilm heterogeneity, as well as to train the spectral data for biofilm predictions.

1. Introduction

Spectral imaging, also known as hyperspectral imaging (HSI), is a powerful technique that provides both spectral and spatial information [1,2]. The HIS-generated data can be analyzed using various chemometric algorithms or machine learning methods [3,4]. This makes spectral imaging a promising choice for heterogeneous samples, as it allows the detection and identification of biological or chemical samples as well as specific compounds of interest [5–10].

The data characteristics in HSI analyses should lead to modifications of aspects related to a reference information, in order to be able to carry out the prediction models [5,11]. However, most reference methods are designed for average spectra of the entire sample and do not consider the spatial variations at the pixel level [5]. Staining is a common practice in histology and medical fields [12–22], microbiology [23–38], microplastics [39], etc. It is used to mark and to identify the substances and units showing specific features on a given surface or object. An important application of this technique, the crystal violet staining for biofilm visualization, was developed by Christensen et al. (1985) [40]. Crystal violet binds to negatively charged functional groups and molecules in a

Abbreviations: DP, Digital photography; FPS, Frames per second; HS, Hyperspectral; HSI, Hyperspectral imaging; HDPE, High-density polyethylene; ROI, Region of interest; TP, true positives; TN, true negatives; FP, false positives; FN, false negatives.

* Corresponding author: lombofelipe@uniovi.es
** Corresponding author: pelayogg@asincar.com
E-mail addresses: lombofelipe@uniovi.es (F. Lombó), pelayogg@asincar.com (P. González).

https://doi.org/10.1016/j.talanta.2023.124655
Received 16 February 2023; Received in revised form 25 April 2023; Accepted 5 May 2023
Available online 12 May 2023

given biofilm, therefore staining the whole biofilm components [41]. In fact, pixelwise information can be obtained by staining such samples and then processing them with the use of digital image treatment methods [42]. When the spectral images of the samples are acquired before staining, the previously referred challenge can be overcome by supplying the pixelwise reference information to the spectral information.

In this sense, in the food industry, spectral imaging techniques can be used for the detection and monitoring of bacterial biofilms, which are organized communities of bacteria embedded in a protective complex, a self-produced extracellular polymeric substances matrix (EPS, exopolysaccharide; proteins, extracellular DNA) [43]. These biofilm bacteria potentially possess an increased resistance to drugs, disinfectants, and environmental factors, in comparison with free-living planktonic microbial cells [44–48] and cause various issues in food processing, such as contamination, spoilage, and reduced shelf life of products [49,50]. Also, in industrial facilities, conventional microbiology techniques are either not applicable or not effective to determine the presence of biofilms. In addition to this, classically, the manufactured food products are tested for several microbiological criteria without prior information of the safety of the production line, and the results of these tests usually become available after several hours or days. This phenomenon causes irreversible damages associated to these food products, in different aspects such as economic and public health issues, as the effects of the presence of a given biofilm may take place during several days or weeks in a production line [51–54].

Regarding this, the application of spectroscopic methods is a promising alternative for rapid analysis, size scalability and its mode transfer capabilities (in-line, at-line) along the production process in a given factory. A key advantage of imaging techniques is that these can help to locate biofilms which are difficult to find in extensive production lines, containing several units or large equipment along the production line.

In this work, spectral imaging is used as primary detection method, using crystal violet staining as a reference method for the detection of biofilms. We have acquired spectral images of biofilms formed on high-density polyethylene coupons (HDPE) in the visible and near-infrared (vis-NIR) range. Crystal violet staining was used as a biofilm indicator, and the treated digital images of stained biofilms were used as a reference. Image processing and artificial neural networks (ANN) methods have been used to overcome challenges caused by biofilm heterogeneity and to train the spectral data for biofilm predictions.

P. aeruginosa, a model facultative Gram-negative bacterium and a priority pathogen, which forms irregular and heterogeneous biofilm structures, has been used here to assure the strength of the method [45–47,55,56]. The chemical composition at the different layers of this bacterium biofilms, and therefore the presence of different substances at different locations of the tested samples are known to be different because of its complex nitrogen and oxygen metabolism [57–59]. The aim of this research is to develop a fast, efficient, and non-invasive analytical method to predict the presence of bacterial biofilms.

2. Materials and methods

2.1. Preparation of biofilms on coupons

The freeze dried *P. aeruginosa* CECT108 strain was reconstituted with tryptic soy broth (TSB, Oxoid, United Kingdom) medium in accordance with the guidelines from the provider (CECT, Valencia, Spain). Cells from overnight grown cultures were dissolved in fresh TSB, including 20% glycerol (VWR, Belgium)) and stored at −80 °C. Prior to use, these stock cryovials (VWR, Belgium) were thawed and used with a sterile loop to create a fresh culture on tryptic soy agar (TSA, Oxoid, United Kingdom) plates. The plates were incubated at 37 °C for 24 h and kept in a fridge at 4 °C. Isolated single colonies were taken from these plates to prepare the overnight cultures.

Biofilms were formed on the horizontal midline of the high-density polyethylene (HDPE, 100mm × 50mm × 3 mm) coupons, just at the culture medium-air interphase (Plastiastur, Spain), growing irregularly also on their upwards sections. Each overnight *Pseudomonas aeruginosa* CECT108 culture in TSB (at 37 °C) was diluted to an absorbance of 0.5 at 550 nm, using a UV–vis spectrophotometer (Biochrom Libra S60, Vidrafoc, Spain) and polystyrene cuvettes (VWR, Belgium). 1 ml of a 1:100 dilution of the standardized bacterial inoculum was added into each individual beaker, which was half-filled with TSB culture medium, and then these suspensions were vortexed. Each sterilized coupon was placed in these suspension beakers. A total of 29 biofilm samples were prepared with this method, and they were incubated at 37 °C for 48 h, as a closed and static conditions system. The coupons contamination was tested with 7 control samples, each for a different beaker, prepared according to a similar procedure in which the bacterial inoculum was omitted.

After incubation, the HDPE coupons were washed with sterile water for 1 min, and then let to air dry. The biofilms generated with the above mentioned shapes remained on the coupons after washing.

2.2. Bacterial cultures

For biofilms preparation, 1 ml of $1{:}10^6$–$1{:}10^8$ dilutions of the standardized inoculum were cultured on tryptic soy agar plates (TSA, Oxoid, United Kingdom), in order to quantify the colony forming units (CFUs) in these inocula. These plates were incubated at 37 °C for 24 h. Different coupons replicates were used for CFUs measurement and for imaging-staining.

After biofilms incubation, 4 randomly chosen biofilm coupons were washed with phosphate-buffered saline (PBS, VWR, Belgium) twice. In the case of the four biofilm samples to be cultivated for CFUs determination, 50 mg of cellulase (MP Biomedicals, USA) was added into 9 ml of PBS in a plastic bottle. The suspension was vortexed and left for half an hour at 37 °C to activate the enzyme, as described by Fleming et al. (2020) [60]. The biofilm on the coupon was then scraped by a sterilized steel razor blade (VWR, Belgium) carrying out 20 downwards strokes into the PBS-enzyme mixture; to recover the biofilm biomass. The final mixture was vortexed and serially diluted at $1{:}10^4$–$1{:}10^8$ dilutions. 100 μL of each dilution was cultured on cetrimide agar (Oxoid, United Kingdom) plates and then incubated at 37 °C for 24 h.

2.3. Acquisition of spectral images

The samples were subjected to HSI with a SPECIM FX-10 camera (400–1000 nm, 5.5 nm spectral resolution, 1024-pixel spatial resolution and 448 spectral bands) (Konica, Finland) (Supplementary Fig. S1). The camera was mounted on a LabScanner (Specim, Konica, Finland) scanner, which had a mobile tray. This configuration was decided to facilitate the camera to work using the push broom line scanning technique: the image lines were captured one by one at a constant speed. HDPE boards with a total thickness of 20 mm were placed under the coupons, to allow that the background of the moving tray was the same material as in the coupons. The hyperspectral line acquisition speed was 50 FPS. The height of the hyperspectral camera above the samples was 227 mm. To calculate the optimum integration time, the Specim White Calibration Tile reference (Konica, Finland) was chosen, in a way that the photon counts at the wavelength where the maximum was near 90% of the detector saturation. The integration time used was 13 ms. The lighting used consisted of two lines of three halogen spotlights of 35 W each, with a total power of 210 W. These lines of lamps were placed on both sides of the hyperspectral camera at an angle of 45° over the line of sight of the camera, so that the light reaching the hyperspectral camera had a diffusive origin.

The capture of the HSIs was carried out using the Lumo Scanner Software (Specim, Konica, Finland) to operate the hyperspectral camera and the scanner. The HSI of two coupons were taken at the same time, to save hard disk memory (100 acquired hyperspectral lines: 80 Mb). 25

samples were imaged and 13 HSIs were taken (12 pairs and 1 individual one). All HSIs were taken in dark conditions. The white imaging reference provided by the manufacturer was used to determine the reference, and the shutter of the camera was closed to prevent the entry of light and to determine dark current. In both cases, 100 spectral lines were taken and averaged, obtaining two vectors of average values that were used to obtain the reflectance values of this HSI by means of:

$$Reflectance = \frac{Measurement - Dark\ Current}{Reference - Dark\ Current} \quad (1)$$

2.4. Crystal violet staining

Biofilm samples were stained to locate the biofilms on the coupons after imaging. Also, the control samples were stained to cross check for eventual contamination.

After the HSI step, the coupons were incubated at 42 °C for 1 h to fix the biofilms. They were stained with a solution of 1.8% crystal violet solution of Gram stain (BioMérieux, France) for 5 min, washed with distilled water three times and let to air dry. During this drying step, the coupons were placed in the same position (the previously liquid submerged incubation section on the lower side and the aerial section on the upper side) as they were being incubated, therefore, some of the excess water was dripping downwards from the coupon.

2.5. Acquisition of digital photographs

DPs (RGB) of the crystal violet-stained biofilm samples were taken with a Canon EOS 1200D camera (Canon, Spain) (Supplementary Figs. S2–S5). The resolution of the photographs was 1920 × 1280. The photographic camera was placed in the scanner in the same position as the hyperspectral camera was. In this case, the mobile tray of the scanner was not used, but the coupons were placed perpendicular to their position when the HSIs were taken, and just below the projection of the camera. The rest of the elements were arranged exactly in the same position. In this way, it was possible to place the ROI of each coupon in the area where the light from the lamps was homogeneous, resulting in a uniform light intensity in a ROI of 60 mm × 45 mm.

2.6. Optical density (OD) measurements

After DP, the stained biofilms were recovered with 33% glacial acetic acid (Labkem, Barcelona, Spain). The optical densities of these dye solutions were measured at 570 nm with a UV–vis spectrophotometer (Biochrom Libra S60, Vidrafoc, Spain), to have an overview of the total biomass of the biofilms that were analyzed by spectral imaging.

2.7. Data treatment and prediction models development

Once the experimental work was carried out and the HSIs and the DPs of the stained biofilms were obtained, we proceeded to treat and to extract the necessary information from those images, in order to create the prediction models for the presence or absence of biofilms. In Fig. 1, a diagram is given for the process of developing the classification models.

Before starting to process the images, the HSIs and DPs data from 7 coupons data were separated from the 25 samples generated. These coupons were not used at any point in the prediction model creation process, but only when the models were developed, for final model testing purposes. The remaining 18 coupons were used for building the prediction models. Specifically, the steps to transform the information from these images into the prediction models were the following ones: points correspondence, homographic transformation and HSIs resizing; collection of the data from the DPs and the transformed HSIs; and application of machine learning algorithms to build the binary classification models using neural networks.

2.7.1. Points correspondence, homographic transformation and HSIs resizing

The issue about creating a relationship among the HSIs and the DPs data is that they are not present in the same position, nor do they have the same resolution. The objective of transforming the HSIs is to achieve a voxels coincidence in the position with the pixels of the stained biofilms DPs. With this transformation, a one-to-one correspondence of the spectral voxels with the pixels of the DPs was achieved, and two images were obtained where each spectrum had its corresponding "analytical" value of one of two-color channels: in this case, the green and red channels of the DP images were studied. The study of the blue channel was dismissed because in the preliminary tests of the prediction models, the results of this channel were notably poorer than the other two.

To achieve a mapping of the points of the HSIs on the DPs, the HSIs were transformed using homography [61], a perspective transformation between two planes through linear mapping. In a 3D space, by means of the so-called homographic matrix, it is possible to transport images between two planes of the space. The source plane was the one corresponding to the HSI's and the destination plane was the one corresponding to the DP's. This homographic matrix was a 3 × 3 matrix, with nine terms, but 8° of freedom (one term was a function of the rest). The transformation between the coordinates of the origin plane and the destination plane was calculated using the following:

$$\begin{bmatrix} x_1' \\ x_2' \\ 1 \end{bmatrix} = \begin{bmatrix} h_{11} & h_{12} & h_{13} \\ h_{21} & h_{22} & h_{23} \\ h_{31} & h_{32} & h_{33} \end{bmatrix} \begin{bmatrix} x_1 \\ x_2 \\ 1 \end{bmatrix} \quad (2)$$

where x_i are the source coordinates (HSIs), x'_i are the destination coordinates (DPs) and h_{ij} are the parameters of the homographic transformation matrix.

To specify this matrix, 4 common points were needed from each of the planes (origin and destination). These points were chosen to be the four corners of the biofilm coupons in both the HSIs and the DPs images (Fig. 2). The coordinates of these points were taken manually. In the case of the HSIs, the monochrome image generated from one wavelength was used. Both the calculation of the homographic transformation matrix and its subsequent use were carried out using the Python openCV package [62]. In addition to apply the homographic transformation to each spectral channel of the HSI, the resolution of the HSI was changed so that it had the same resolution as the digital image and thus it was achieved a correspondence between voxels and pixels. To achieve the change in resolution, two common methods were used: the bilinear and the bicubic interpolation methods. In the bilinear interpolation, in order to know the value of each pixel of the interpolated image, the values of four adjacent pixels were used and the value of the new pixel was calculated as the weighted average of these four pixels. The bicubic interpolation is the natural evolution of the bilinear interpolation when more pixels are used in the interpolation. In this study, the closest 4 × 4 pixels were used (16 pixels in total). The value of the new pixels from two cubic interpolations (horizontal and vertical) were obtained by this interpolation method.

After these operations, on one side, there was a set of DPs and on the other, a set of transformed HSIs with the same resolution as the digital images, and where the data occupy the same coordinates as the DPs.

2.7.2. Collecting data from the DPs and the transformed HSIs

The next step was to collect voxels from all the images to create a training data set for mathematical modelling. For this, it was necessary to set a region of interest (ROI) on each coupon, which was the place where the voxels were extracted. This region of interest was a rectangular area of the coupon that was 2.5 mm from the short sides (5% longer in their right and left directions) and 20 mm from the long sides (20% longer areas in upper and lower sides), to avoid the edges of the coupon, since crystal violet easily adheres to edges and tears, even in the

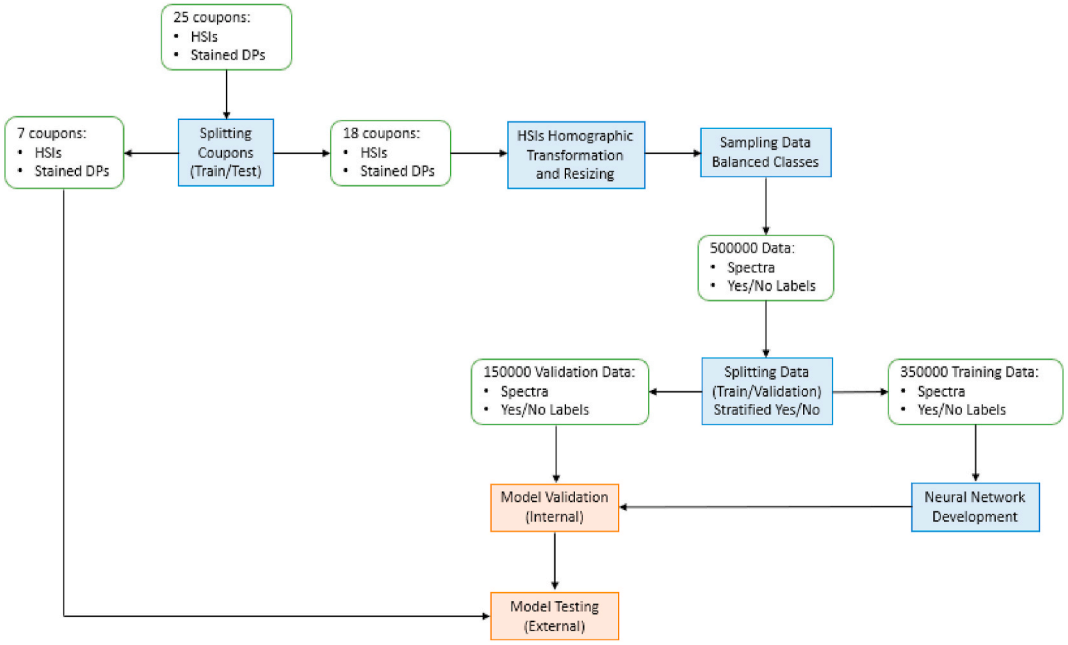

Fig. 1. Overview of the data analysis methodology.

absence of biofilm, consequently causing false positives in these images (Fig. 3). The long side of the coupon was reduced to a greater extent than the short side because it was rare to find biofilm at the ends of the long side of the coupon (biofilm was usually found in the center of the coupon, at the culture medium/air interphase), and by removing this part, it was possible to focus on a mixed area with the pixels, where biofilm was found and where it was not. Thus, this ROI was a rectangle 60 mm long and 45 mm wide that was centered on the coupons (Fig. 3). In order to delimit this area, a mask was applied that eliminated everything that was outside this ROI. All the voxels that were within the ROI of the coupons were likely to be chosen to carry out the prediction model. The voxel selection process was carried out independently for the green and red channels, obtaining as a result data sets for both channels.

The first step in choosing the pixels was to create a database containing all the information regarding the pixels (of the stained biofilm DPs) of ROIs of all the coupons. This information included coupon identity, image coordinates (X–Y) of the pixels in the image, and color intensity values in the green or red channel.

Then, a threshold was chosen that separated the classes (with biofilm and without biofilm), so that the pixels with values lower than this threshold were labelled as “positive” for the presence of biofilm and those with higher values were labelled as “negative” for the absence of biofilm. The range of thresholds for which the data sets were constructed was uniformly distributed (Fig. 4) in the area where the lowest intensity values of the histograms of the coupons without biofilm (control) were found. At the lower values of these intensities, pixels with stained biofilm were found. There was an overlapped area between both regions, which was the study area. The following three thresholds were chosen for each color channel:

- Green: 105, 110, 115
- Red: 175, 180, 185

Each color threshold separated its corresponding histogram into two regions with their associated pixels. The ROI data set for all coupons was divided into two sets. These sets did not have the same number of pixels. They varied in the number of elements depending on the threshold value, being especially unbalanced for the lower thresholds.

When this classification model was being created, it was recommended to balance the data at different classes. In this case, since the number of available pixels was very high, it was decided to extract a sample of sufficiently large data, in a way that they were representative of the complete set of data. These sets contained 250,000 pixels for each of the positive and negative classes. The pixels were chosen uniformly

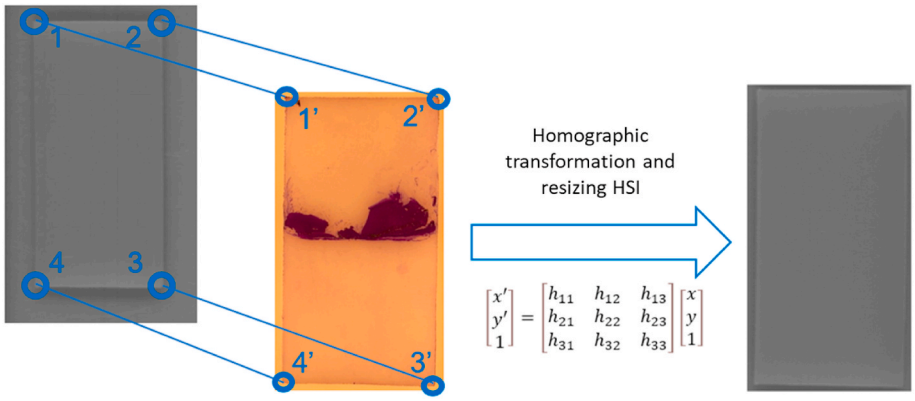

Fig. 2. Representation of size matching between HSI and DP.

for all the color intensities present in each class, representative of the intensity range.

As a summary, at the end of this pixel sampling process, a data set (500,000 positive/negative labels and spectra pairs) was obtained for each of the two-color channels. Two interpolation methods and three thresholds applied to each color. In total, 12 sets of spectra with their corresponding values of presence/absence of biofilm were used to create the machine learning models.

2.7.3. Machine learning algorithms to build the binary classification models: neural networks

A neural networks method was used to establish the relationship between the spectra of the voxels of the HSIs and the presence or absence of a biofilm, as a function of the thresholds of color channels of the DPs of the stained biofilms.

The first step in the creation of these prediction models was to divide the training set into two prediction and validation model development subsets, with 70% and 30% of the data, respectively. The data were divided randomly, but in a stratified way, based on the class. The neural networks were trained with the training data and the validation set was used to know the error in a set of pixels not used in the neural network training. The difference with the data from the test coupons was that validation pixels came from the same coupons than the pixels that were extracted for training neural networks. They could be considered as an internal test of the prediction model.

The training of the neural networks has been carried out using the tools provided by the Scikit-Learn package [63]. For data pre-treatment, a standardization was used, obtaining independent variables with a mean value of zero and a standard deviation of value of one (the typical pre-treatment of neural networks). In the preliminary tests, more types of pre-treatments such as standard normal variate (SNV), multiplicative scatter correction (MSC), Detrending or Savitzky-Golay derivative [64] were tested, but no improvements were obtained. The neural network model developed to perform the classification was a multilayer perceptron, with a hidden layer of 30 hidden neurons. Neural architectures with more hidden neurons were tested, but better results were not achieved in those cases. The hidden neurons had rectified linear units (ReLU) activation function, and the output neuron had the sigmoid function as activation function. To perform the optimization of neuronal weights, the Adam optimization algorithm [65] was used.

The following four metrics were used in order to assess the performance of neural networks models both for training and test:

- Accuracy, as a fraction of correct predictions (both positive and negative biofilm):

$$\text{Accuracy} = \frac{TP + TN}{TP + TN + FP + FN} \tag{3}$$

- Precision, as a fraction of positive (biofilm positive) predictions that are correct:

$$\text{Precision} = \frac{TP}{TP + FP} \tag{4}$$

- Recall, as a fraction of actual positives that are correct:

$$Recall = \frac{TP}{TP + FN} \tag{5}$$

- Specificity, as a fraction of actual negatives (biofilm negative) that are correct:

$$\text{Specificity} = \frac{TN}{TN + FP} \tag{6}$$

3. Results and discussion

Control samples did not show any turbidity in the incubated medium nor biofilm-like stained areas on the coupons. The standardized overnight suspension contained 6.4×10^8 CFU/ml. The cultured four biofilms replicas had an average of 6.5×10^7 CFU/ml and standard deviations of 1.74, 2.49, 1.59 and 0.79. The OD values of the stained samples are provided in supplementary information, Table S1..

Data pairs of spectra extracted from the HSIs, and the true/false biofilm labels extracted DPs of the 18 coupons were first randomly resampled to obtain equal number of "yes" and "no" reference data for biofilm presence. Then, with a split of 70% training and 30% validation data, they were subjected to ANN model building. The results between 12 groups (2 types of color channels, red and green, from which the stained biofilm coupon pixel intensity values were extracted, the 2 types of interpolation method performed in the transformation of the HSIs, and the 3 thresholds for each channel) were compared in terms of metrics as accuracy, precision, recall and specificity (Supplementary Table S4). With use of bilinear interpolation, better models were achieved. These results are represented in Supplementary Table S5 and Fig. S6. Another point to mention here is that the models may present low overfitting because the data used in the training of neural networks (70%) and the data used in validation (30%) present very similar metrics in all the models created.

The bilinear interpolation models were chosen to be applied on the 7 previously unused test coupons, as this method was demonstrated to be better than bicubic interpolation. The entire dataset from all the voxels of ROIs in the 7 training coupons was used for testing (each voxel of the entire test coupons individually, unbalanced data). The average metrics from these 7 unbalanced test coupons and from 18 unbalanced training data was obtained for comparison. The red channel showed similar but slightly better metrics than the green channel. Similar results were also obtained from the three thresholds used. The details of these results are presented in Tables 1 and 2. To simplify the representation and

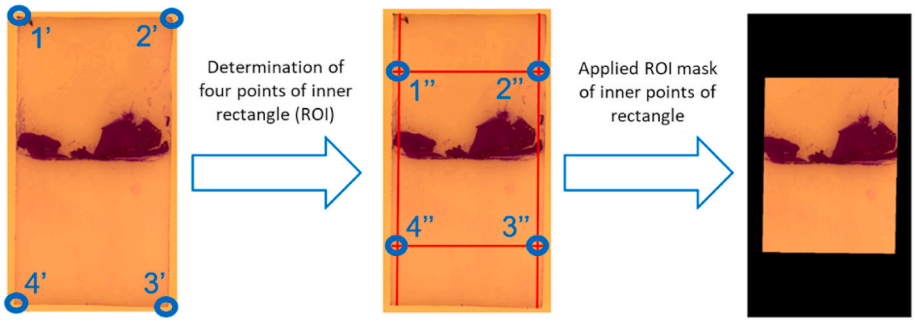

Fig. 3. Selection of ROI and masking of DPs.

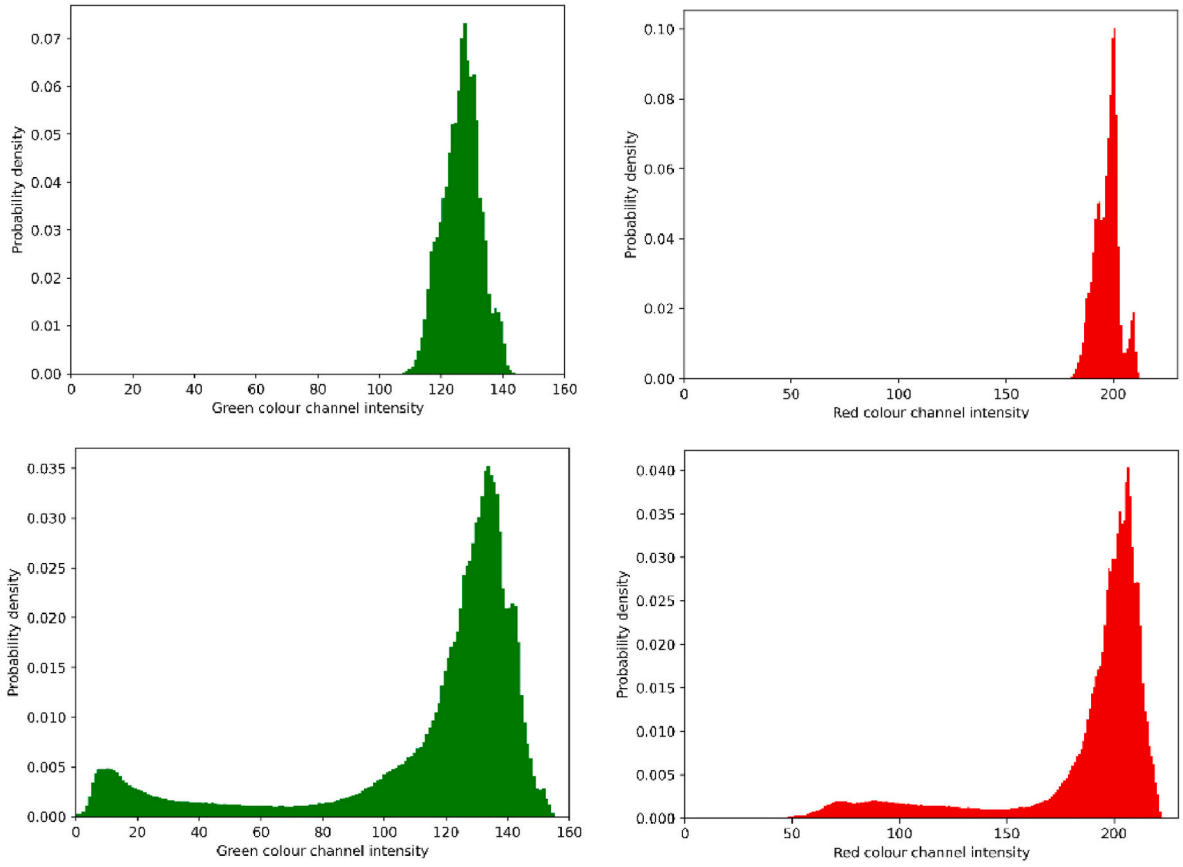

Fig. 4. Histograms of green and red color channels in the ROI of coupons for contamination control free of biofilms (upper) and biofilms (lower).

Table 1
Green channel results (DP) using bilinear interpolation for the unbalanced voxels of individual test coupons (mean for training and testing).

Coupon	Threshold	Accuracy	Precision	Recall	Specificity
1	105	0.944	0.684	0.947	0.944
1	110	0.938	0.725	0.898	0.945
1	115	0.925	0.787	0.801	0.952
2	105	0.921	0.931	0.669	0.987
2	110	0.890	0.951	0.587	0.990
2	115	0.842	0.951	0.518	0.988
3	105	0.925	0.958	0.713	0.990
3	110	0.911	0.973	0.681	0.993
3	115	0.899	0.981	0.670	0.995
4	105	0.635	0.393	0.998	0.522
4	110	0.636	0.420	0.996	0.507
4	115	0.652	0.467	0.991	0.504
5	105	0.950	0.786	0.987	0.942
5	110	0.955	0.823	0.976	0.950
5	115	0.954	0.841	0.961	0.953
6	105	0.869	0.847	0.813	0.905
6	110	0.865	0.852	0.827	0.893
6	115	0.843	0.836	0.822	0.861
7	105	0.931	0.888	0.796	0.971
7	110	0.915	0.918	0.739	0.977
7	115	0.892	0.913	0.707	0.971
Mean Test	105	0.883	0.785	0.846	0.895
Mean Test	110	0.873	0.810	0.814	0.894
Mean Test	115	0.859	0.826	0.781	0.890
Mean Training	105	0.900	0.750	0.843	0.913
Mean Training	110	0.892	0.777	0.823	0.914
Mean Training	115	0.873	0.789	0.801	0.905

Table 2
Red channel results (DP) using bilinear interpolation for unbalanced voxels of individual test coupons (mean for training and testing).

Coupon	Threshold	Accuracy	Precision	Recall	Specificity
1	175	0.950	0.643	0.971	0.948
1	180	0.946	0.662	0.960	0.944
1	185	0.944	0.720	0.917	0.948
2	175	0.938	0.948	0.678	0.992
2	180	0.908	0.954	0.604	0.992
2	185	0.850	0.958	0.500	0.991
3	175	0.934	0.876	0.738	0.977
3	180	0.932	0.927	0.731	0.985
3	185	0.924	0.954	0.718	0.989
4	175	0.681	0.385	0.998	0.603
4	180	0.651	0.381	0.998	0.555
4	185	0.622	0.386	0.997	0.505
5	175	0.943	0.744	0.988	0.935
5	180	0.947	0.764	0.989	0.938
5	185	0.957	0.814	0.983	0.951
6	175	0.864	0.837	0.745	0.926
6	180	0.862	0.835	0.776	0.911
6	185	0.856	0.834	0.804	0.892
7	175	0.940	0.875	0.792	0.974
7	180	0.938	0.873	0.809	0.970
7	185	0.926	0.876	0.787	0.967
Mean Test	175	0.893	0.759	0.844	0.908
Mean Test	180	0.884	0.772	0.838	0.900
Mean Test	185	0.869	0.793	0.815	0.893
Mean Training	175	0.923	0.759	0.847	0.935
Mean Training	180	0.913	0.771	0.831	0.931
Mean Training	185	0.899	0.793	0.805	0.929

interpretation of results, the following discussion from here onwards is focused on the red channel and the threshold value of 180.

Fig. 5 shows such results at the referred settings (red channel, threshold value of 180 and bilinear method), using unbalanced data split from all pixels in the ROIs. The Supplementary Fig. S7 shows the values for green channel. Supplementary Information Tables S2 and S3 show

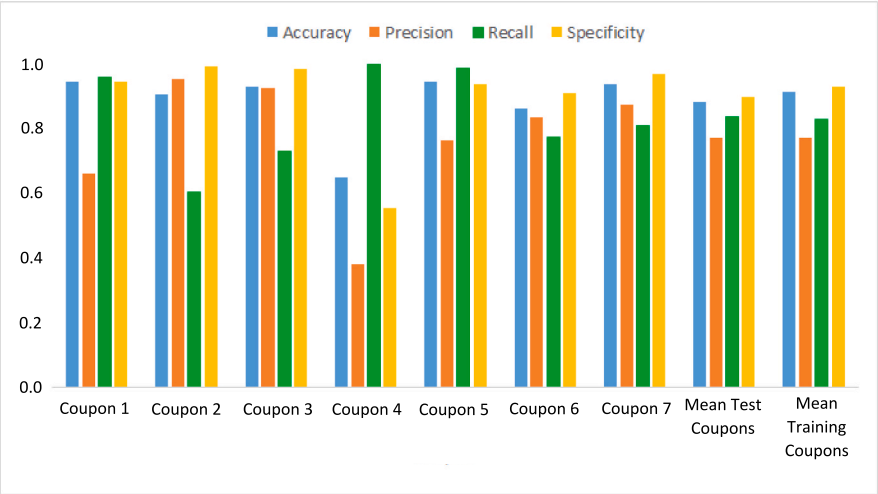

Fig. 5. Metrics for ANN model results (unbalanced data) of the red channel with a threshold value of 180 for the test coupons, their mean values and the mean values for training set.

the values for training coupons, individually. The mean values of the metrics for the training set (validation set of neural network models, referred as "mean training" in the histogram) and those of the test set (external test, referred as "mean test") had similar values, indicating that the model is able to generalize to test predictions. The expected change was observed in the case of the coupons resampled with random pixel selection (to get a balanced amount of data for "yes" and "no" classes of biofilm presence) with respect to these same coupons evaluating all the voxels in the ROIs in training (unbalanced) coupons. Unbalancing the data actually increased the accuracy and the specificity, and also decreased the precision and the recall.

Regarding the metrics of the individual coupons in Fig. 5, it was observed that they had a lot of variability with respect to the average metrics. In the test set, coupons 3, 5, 6 and 7 showed similar or slightly different values to the average. The other cases showed more significant deviations, obtaining higher values of recall and lower precision, as in the cases of coupons 1 and 4; or high precision and low recall, as in the case of coupon 2. The greatest source of impact on this variability of the metric values may be crystal violet staining, which is a qualitative method and depends on the treatment carried out on each specific coupon. In addition, another source of variability may be that having more or fewer pixels with values close to the threshold, these pixels may become more susceptible to misclassification than coupons with pixels further away, after using the neural network model.

In Fig. 6, three ROI images for each of the 7 test coupons are shown: the real image (red channel, left image), the image obtained after applying the class separation threshold (for the red color channel) (center image), and after applying a class prediction of HSI using the corresponding neural network model (180 threshold) (right image). The models were trained with resampled data as randomized and balanced data split; tested on the entire test coupons. The areas with biofilms are visible in the central region of the coupons images (blue color in the left images). These images can be used to track how the metrics were influenced by the developed method.

The accuracy provides the total prediction successes (positive and negative) of the model in the ROI of the image, as a general metric. There are two relationships that provide information that are used to evaluate the model when applied to an HSI: the precision and recall relationship, and the recall and specificity relationship. The relationship between precision and recall in this case is related to the predictions of the positive class (biofilm presence). Thus, when one (precision or recall) decreases the other increases, and vice versa. The variation in this relationship is evident, especially in the area where the biofilms are found. Also, even more positive class predictions are made, as a comparison of the number of brighter pixels in the predicted image (right images) and to the bright pixels in the threshold reference image (center image). As the precision increases, fewer false predicted positives will be seen in the biofilm area.

As the recall increases, the density of pixels that are true positives will increase. The relationship between recall and specificity is the balance between accuracy among true positives and accuracy among true negatives. In this case, the specificity is usually more stable than the precision, and its value begins to decrease only when false positives appear in areas away from the biofilm. The precision/recall relationship is like "fine-tuning" (the biofilm area) detection, and the recall/specificity relationship is a more general description.

Some of the issues related to the difficulty in modelling around the established threshold values can be due to the presence of nascent (or weak) biofilms. The more biofilm is present on the coupons, the darker the pixel intensity (crystal violet) is. Therefore, the stronger the biofilm was in these experiments, the easier it was to be detected. Also, from the microbiological side, the accumulative effects of substances present in the biofilm extracellular matrix and in the bacterial cells, as well as the metabolism and interaction of some of these substances (containing nitrogen, oxygen, hydrogen, etc.) might have contributed to the overall spectral profiles in visible and near infrared region. All the samples were expected to contain an aerobic *Pseudomonas aeruginosa* biofilm layer. In the case of a thicker biofilm matrix, the lower layers were expected to be anaerobic, according to previously reported studies [57–59].

In addition, as *Pseudomonas aeruginosa* biofilms seemed to form biofilms of differing thickness or intensity, location-wise, therefore, the spectral samples differed even within the same coupon sample. Therefore, the varying thicknesses of the anaerobic *P. aeruginosa* biofilm layer (deeper layers) and the aerobic layer (surface layers) might have caused changes in the compositions of bacterial metabolism input and outputs, proteins and polymers present in the biofilms. This may have affected the content of chemical bonds made of organic substances location-wise, and thus the spectra of the pixels on hyperspectral images.

Finally, crystal violet staining might have led to false reference labels at some pixels. Namely, some of the false positives may be the result of an excess of water slightly mixed with the dye, due to the presence of strong biofilm areas, which used to drop downwards on the coupon and to dry on the non-biofilm area, during samples drying step. A similar phenomenon can be encountered when the HDPE polymer absorbs media and/or crystal violet. Conversely, given that crystal violet staining is a qualitative method, some false negatives may have been

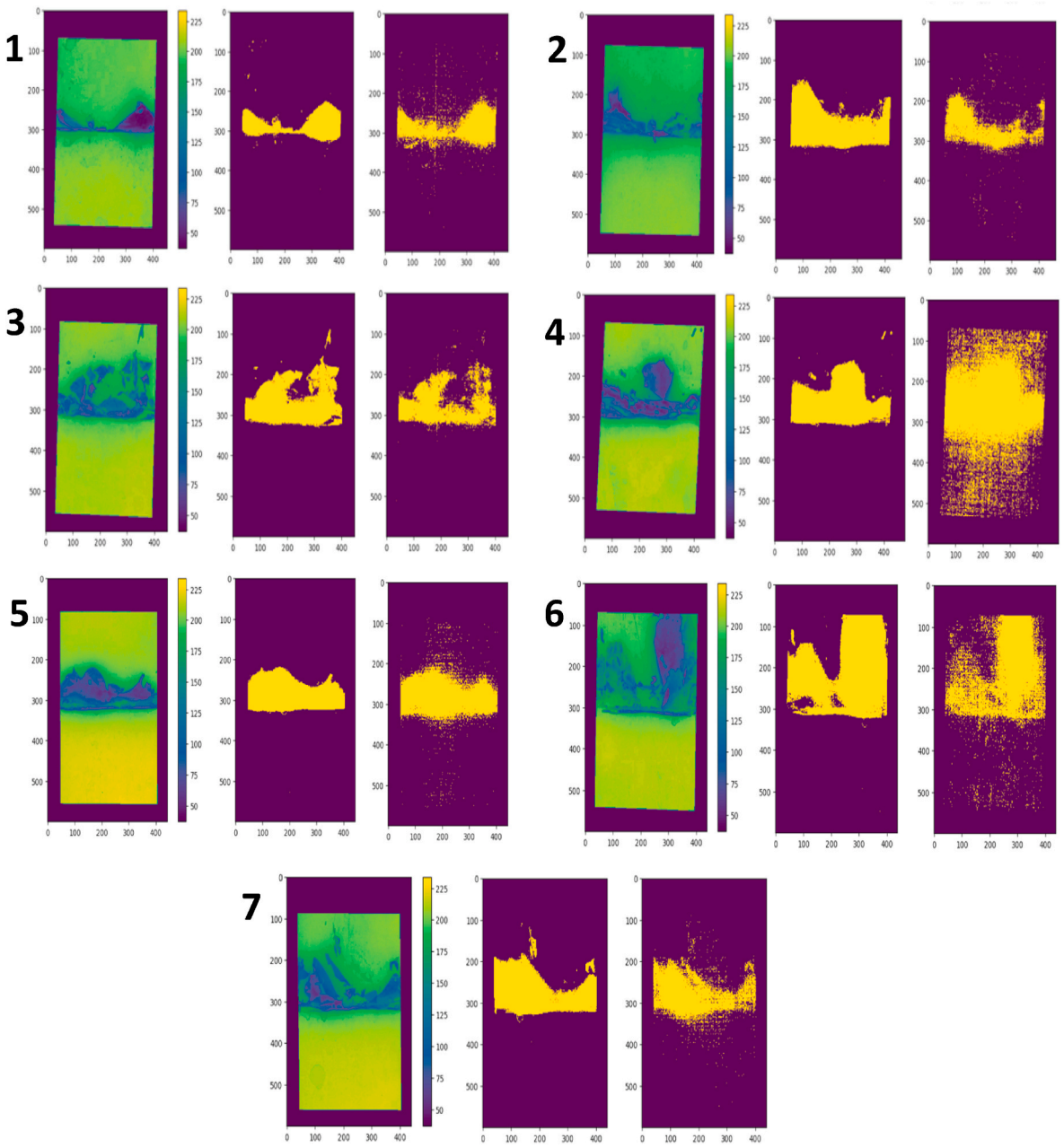

Fig. 6. ROI of the test coupons, left: real image, middle: DP data subjected to class separation of red color channel pixels at the intensity of 180 (threshold), right: class predictions on spectral data by neural network model. 1: Test coupon 1; 2: test coupon 2; 3: test coupon 3; 4: test coupon 4; 5: test coupon 5; 6: test coupon 6; 7: test coupon 7.

generated from the areas with a biofilm matrix, as sessile cells can be slightly removed during the washing steps in the staining process, together with the excess dye. This may have occurred, even though the coupons have been subjected to a heat pretreatment step (att 42 °C). This generation of false negatives has been already reported by Azeredo et al. (2017) [36]. However, even if these last three issues may have occurred, they did not pose a significant problem in the overall prediction performance of the developed method (weak biofilms or intensities aside).

4. Conclusion and future perspectives

In overall, the described method allows to predict the presence of biofilm in each voxel of a spectral image from a HDPE surface, via a mathematical model.

Although *P. aeruginosa* is a well-researched bacterium in biofilm studies, due to its importance and ability to easily form strong biofilms on various surfaces, including HDPE, it may not be the easiest one to generate the machine learning models in spectroscopic detection studies like this. The reason for this can be summarized as the presence of high sample-to-sample irregularities, because of the *P. aeruginosa* biofilm structure, the background interference of the plastic polymeric surface (HDPE) to the biofilm polymers and the noise associated to the remote sensing settings of the camera. However, the generated models in this work are able to tackle these issues well and they have a good prediction ability. Therefore, the modelling results of this work show that the method has been able to perform well even in the presence of these intrinsic issues.

The described method is found promising to further extend the development of biofilm detection methods to other bacterial species

(*Escherichia coli, Salmonella enterica, Bacillus cereus*) and substrates (stainless steel, glass). In the case of biofilms, a model building strategy for the prediction of the presence of a specific matrix component or a specific microorganism, can be tested using spectral imaging. Lastly, this method might further be useful in cases where it may be feasible to stain samples, whether they are biofilms or not.

Credit author statement

Funding acquisition (PG, FL), Investigation (NA, MFH); Supervision (PG, FL); Writing – original draft (NA, MFH); Writing – review & editing (FL). All authors read and approved the final manuscript.

Declaration of competing interest

The authors declare the following financial interests/personal relationships which may be considered as potential competing interests: J. L. Gomez Martin reports financial support was provided by Government of the Junta de Extremadura (Autonomous Region, Spain). Felipe Lombo reports financial support was provided by Government of the Principality of Asturias (Autonomous Region, Spain). L. Fernandez-Calleja, M. Garcia-Dominguez, J.L. Gomez Martin, C.J. Villar, F. Lombo has patent #P202130363, COMPUESTO BIOACTIVO EXTRAÍDO A PARTIR DE PHLOMIS PURPÚREA, MÉTODO DE OBTENCIÓN, COMPOSICIÓN ANTIFÚNGICA QUE LO CONTIENE Y SU USO issued to N/A. N/A.

Data availability

Data will be made available on request.

Acknowledgements

This work was funded by H2020 Marie Skłodowska-Curie ITN, Break Biofilms Project No. 813439. Authors wish to thank *Ayudas a organismos públicos para apoyar las actividades de I+D+I de sus grupos de investigación* (AYUD/2021/51347) from Principado de Asturias (Spain) as well.

Appendix A. Supplementary data

Supplementary data to this article can be found online at https://doi.org/10.1016/j.talanta.2023.124655.

References

[1] G. Foca, C. Ferrari, A. Ulrici, G. Sciutto, S. Prati, S. Morandi, M. Brasca, P. Lavermicocca, S. Lanteri, P. Oliveri, The potential of spectral and hyperspectral-imaging techniques for bacterial detection in food: a case study on lactic acid bacteria, Talanta 153 (2016) 111–119, https://doi.org/10.1016/j.talanta.2016.02.059.

[2] D. Klein, R. Breuch, J. Reinmüller, C. Engelhard, P. Kaul, Investigation and rapid discrimination of food-related bacteria under stress treatments using IR microspectroscopy, Foods 10 (2021) 1850, https://doi.org/10.3390/foods10081850.

[3] J.A. Fernández Pierna, P. Vermeulen, D. Eylenbosch, J. Burger, B. Bodson, P. Dardenne, V. Baeten, Chemometrics in NIR hyperspectral imaging: theory and applications in the agricultural crops and products sector, in: Comprehensive Chemometrics, Elsevier, 2020, pp. 361–379, https://doi.org/10.1016/B978-0-12-409547-2.14811-5.

[4] R. Qiu, Y. Zhao, D. Kong, N. Wu, Y. He, Development and comparison of classification models on VIS-NIR hyperspectral imaging spectra for qualitative detection of the Staphylococcus aureus in fresh chicken breast, Spectrochim. Acta Mol. Biomol. Spectrosc. 285 (2023), 121838, https://doi.org/10.1016/j.saa.2022.121838.

[5] M. Manley, Near-infrared spectroscopy and hyperspectral imaging: non-destructive analysis of biological materials, Chem. Soc. Rev. 43 (2014) 8200–8214, https://doi.org/10.1039/C4CS00062E.

[6] M.J. Baker, J. Trevisan, P. Bassan, R. Bhargava, H.J. Butler, K.M. Dorling, P. R. Fielden, S.W. Fogarty, N.J. Fullwood, K.A. Heys, C. Hughes, P. Lasch, P. L. Martin-Hirsch, B. Obinaju, G.D. Sockalingum, J. Sulé-Suso, R.J. Strong, M. J. Walsh, B.R. Wood, P. Gardner, F.L. Martin, Using Fourier transform IR spectroscopy to analyze biological materials, Nat. Protoc. 9 (2014) 1771–1791, https://doi.org/10.1038/nprot.2014.110.

[7] X. Li, M. Cai, M. Li, X. Wei, Z. Liu, J. Wang, K. Jia, Y. Han, Combining Vis-NIR and NIR hyperspectral imaging techniques with a data fusion strategy for the rapid qualitative evaluation of multiple qualities in chicken, Food Control 145 (2023), 109416, https://doi.org/10.1016/j.foodcont.2022.109416.

[8] E.D. Spyrelli, O. Ozcan, F. Mohareb, E.Z. Panagou, G.-J.E. Nychas, Spoilage assessment of chicken breast fillets by means of fourier transform infrared spectroscopy and multispectral image analysis, Curr. Res. Food Sci. 4 (2021) 121–131, https://doi.org/10.1016/j.crfs.2021.02.007.

[9] A. Gowen, C. Odonnell, P. Cullen, G. Downey, J. Frias, Hyperspectral imaging – an emerging process analytical tool for food quality and safety control, Trends Food Sci. Technol. 18 (2007) 590–598, https://doi.org/10.1016/j.tifs.2007.06.001.

[10] J.-L. Xu, A. Herrero-Langreo, S. Lamba, M. Ferone, A.G.M. Scannell, V. Caponigro, A.A. Gowen, Characterisation and classification of foodborne bacteria using reflectance FTIR microscopic imaging, Molecules 26 (2021) 6318, https://doi.org/10.3390/molecules26206318.

[11] M. Eady, G. Setia, B. Park, Detection of Salmonella from chicken rinsate with visible/near-infrared hyperspectral microscope imaging compared against RT-PCR, Talanta 195 (2019) 313–319, https://doi.org/10.1016/j.talanta.2018.11.071.

[12] E.I. Yakupova, L.G. Bobyleva, I.M. Vikhlyantsev, A.G. Bobylev, Congo Red and amyloids: history and relationship, Biosci. Rep. 39 (2019), https://doi.org/10.1042/BSR20181415. BSR20181415.

[13] M. Bogdani, Role of immunohistochemical detection of BRCA1 in breast cancer, in: Handbook of Immunohistochemistry and in Situ Hybridization of Human Carcinomas, Elsevier, 2002, pp. 371–384, https://doi.org/10.1016/S1874-5784(04)80048-5.

[14] B.D.C. Vidal, M.L.S. Mello, Toluidine blue staining for cell and tissue biology applications, Acta Histochem. 121 (2019) 101–112, https://doi.org/10.1016/j.acthis.2018.11.005.

[15] M. Salvi, N. Michielli, F. Molinari, Stain Color Adaptive Normalization (SCAN) algorithm: separation and standardization of histological stains in digital pathology, Comput. Methods Progr. Biomed. 193 (2020), 105506, https://doi.org/10.1016/j.cmpb.2020.105506.

[16] J.-L. Wang, L. Zhao, M.-Q. Li, W.-G. Chen, C.-J. Xu, A sensitive and reversible staining of proteins on blot membranes, Anal. Biochem. 592 (2020), 113579, https://doi.org/10.1016/j.ab.2020.113579.

[17] K.S. Yi, C.-H. Choi, C. Jung, Y. Lee, C.-Y. Jeon, H.-G. Yeo, Y. Ahn, J. Hwang, H. J. Lee, J. Cho, B. Kwak, K.A. Kwak, S.-R. Lee, S.-H. Cha, Which pathologic staining method can visualize the hyperacute infarction lesion identified by diffusion MRI?: a comparative experimental study, J. Neurosci. Methods 344 (2020), 108838, https://doi.org/10.1016/j.jneumeth.2020.108838.

[18] M. Lai, B. Lü, Tissue preparation for microscopy and histology, in: Comprehensive Sampling and Sample Preparation, Elsevier, 2012, pp. 53–93, https://doi.org/10.1016/B978-0-12-381373-2.00070-3.

[19] M. Hayashi, T. Sofuni, M. Ishidate, An application of Acridine Orange fluorescent staining to the micronucleus test, Mutat. Res. Lett. 120 (1983) 241–247, https://doi.org/10.1016/0165-7992(83)90096-9.

[20] M.D. Creager, J. Choi, J.D. Hutcheson, E. Aikawa, 3.18 immunohistochemistry, in: Comprehensive Biomaterials II, Elsevier, 2017, pp. 387–405, https://doi.org/10.1016/B978-0-12-803581-8.09828-3.

[21] K.M. McKinnon, Flow cytometry: an overview, CP in Immunol. (2018) 120, https://doi.org/10.1002/cpim.40.

[22] G. Lei, Y. Xia, D.-H. Zhai, W. Zhang, D. Chen, D. Wang, StainCNNs: an efficient stain feature learning method, Neurocomputing 406 (2020) 267–273, https://doi.org/10.1016/j.neucom.2020.04.008.

[23] R.M. Donlan, Biofilms: microbial life on surfaces, Emerg. Infect. Dis. 8 (2002) 881–890, https://doi.org/10.3201/eid0809.020063.

[24] L. Netuschil, T.M. Auschill, A. Sculean, N.B. Arweiler, Confusion over live/dead stainings for the detection of vital microorganisms in oral biofilms - which stain is suitable? BMC Oral Health 14 (2014) 2, https://doi.org/10.1186/1472-6831-14-2.

[25] T. Petrachi, E. Resca, M. Piccinno, F. Biagi, V. Strusi, M. Dominici, E. Veronesi, An alternative approach to investigate biofilm in medical devices: a feasibility study, IJERPH 14 (2017) 1587, https://doi.org/10.3390/ijerph14121587.

[26] P. Ommen, N. Zobek, R.L. Meyer, Quantification of biofilm biomass by staining: non-toxic safranin can replace the popular crystal violet, J. Microbiol. Methods 141 (2017) 87–89, https://doi.org/10.1016/j.mimet.2017.08.003.

[27] J.A. Tantray, S. Mansoor, R.F.C. Wani, N.U. Nissa, Gram staining of bacteria, in: Basic Life Science Methods, Elsevier, 2023, pp. 181–183, https://doi.org/10.1016/B978-0-443-19174-9.00043-X.

[28] X. Zhou, Y. Li, Techniques for oral microbiology, in: Atlas of Oral Microbiology, Elsevier, 2015, pp. 15–40, https://doi.org/10.1016/B978-0-12-802234-4.00002-1.

[29] G.D. Christensen, W.A. Simpson, A.L. Bisno, E.H. Beachey, Adherence of slime-producing strains of Staphylococcus epidermidis to smooth surfaces, Infect. Immun. 37 (1982) 318–326, https://doi.org/10.1128/iai.37.1.318-326.1982.

[30] M. Rüger, G. Bensch, R. Tüngler, U. Reichl, A flow cytometric method for viability assessment of *Staphylococcus aureus* and *Burkholderia cepacia* in mixed culture, Cytometry 81A (2012) 1055–1066, https://doi.org/10.1002/cyto.a.22219.

[31] S.C. Becerra, D.C. Roy, C.J. Sanchez, R.J. Christy, D.M. Burmeister, An optimized staining technique for the detection of Gram positive and Gram negative bacteria within tissue, BMC Res. Notes 9 (2016) 216, https://doi.org/10.1186/s13104-016-1902-0.

[32] Y. Shen, S. Stojicic, M. Haapasalo, Bacterial viability in starved and revitalized biofilms: comparison of viability staining and direct culture, J. Endod. 36 (2010) 1820–1823, https://doi.org/10.1016/j.joen.2010.08.029.

[33] S.Y. Park, C.G. Kim, A comparative study of three different viability tests for chemically or thermally inactivated Escherichia coli, Environ. Eng. Res. 23 (2018) 282–287, https://doi.org/10.4491/eer.2017.223.

[34] M.J. Franklin, C. Chang, T. Akiyama, B. Bothner, New technologies for studying biofilms, in: M. Ghannoum, M. Parsek, M. Whiteley, P.K. Mukherjee (Eds.), Microbial Biofilms, ASM Press, Washington, DC, USA, 2015, pp. 1–32, https://doi.org/10.1128/9781555817466.ch1.
[35] K. Welch, Y. Cai, M. Strømme, A method for quantitative determination of biofilm viability, J. Forensic Biomech. 3 (2012) 418–431, https://doi.org/10.3390/jfb3020418.
[36] J. Azeredo, N.F. Azevedo, R. Briandet, N. Cerca, T. Coenye, A.R. Costa, M. Desvaux, G. Di Bonaventura, M. Hébraud, Z. Jaglic, M. Kačániová, S. Knøchel, A. Lourenço, F. Mergulhão, R.L. Meyer, G. Nychas, M. Simões, O. Tresse, C. Sternberg, Critical review on biofilm methods, Crit. Rev. Microbiol. 43 (2017) 313–351, https://doi.org/10.1080/1040841X.2016.1208146.
[37] C. Wilson, R. Lukowicz, S. Merchant, H. Valquier-Flynn, J. Caballero, J. Sandoval, M. Okuom, C. Huber, T.D. Brooks, E. Wilson, B. Clement, C.D. Wentworth, A. E. Holmes, Quantitative and qualitative assessment methods for biofilm growth: a mini-review, Res Rev J Eng Technol 6 (2017). http://www.rroij.com/open-access/quantitative-and-qualitative-assessment-methods-for-biofilm-growth-a-minireview-.pdf.
[38] M. Klinger-Strobel, H. Suesse, D. Fischer, M.W. Pletz, O. Makarewicz, A novel computerized cell count algorithm for biofilm analysis, PLoS One 11 (2016), e0154937, https://doi.org/10.1371/journal.pone.0154937.
[39] S. Konde, J. Ornik, J.A. Prume, J. Taiber, M. Koch, Exploring the potential of photoluminescence spectroscopy in combination with Nile Red staining for microplastic detection, Mar. Pollut. Bull. 159 (2020), 111475, https://doi.org/10.1016/j.marpolbul.2020.111475.
[40] G.D. Christensen, W.A. Simpson, J.J. Younger, L.M. Baddour, F.F. Barrett, D. M. Melton, E.H. Beachey, Adherence of coagulase-negative staphylococci to plastic tissue culture plates: a quantitative model for the adherence of staphylococci to medical devices, J. Clin. Microbiol. 22 (1985) 996–1006, https://doi.org/10.1128/jcm.22.6.996-1006.1985.
[41] C.I. Amador, R.O. Stannius, H.L. Røder, M. Burmølle, High-throughput screening alternative to crystal violet biofilm assay combining fluorescence quantification and imaging, J. Microbiol. Methods 190 (2021), 106343, https://doi.org/10.1016/j.mimet.2021.106343.
[42] C. Larimer, E. Winder, R. Jeters, M. Prowant, I. Nettleship, R.S. Addleman, G. T. Bonheyo, A method for rapid quantitative assessment of biofilms with biomolecular staining and image analysis, Anal. Bioanal. Chem. 408 (2016) 999–1008, https://doi.org/10.1007/s00216-015-9195-z.
[43] H.-C. Flemming, T.R. Neu, D.J. Wozniak, The EPS matrix: the "house of biofilm cells,", J. Bacteriol. 189 (2007) 7945–7947, https://doi.org/10.1128/JB.00858-07.
[44] T. Rasamiravaka, Q. Labtani, P. Duez, M. El Jaziri, The Formation of biofilms by *Pseudomonas aeruginosa*: a review of the natural and synthetic compounds interfering with control mechanisms, BioMed Res. Int. (2015), e759348, https://doi.org/10.1155/2015/759348, 2015.
[45] M.T.T. Thi, D. Wibowo, B.H.A. Rehm, Pseudomonas aeruginosa biofilms, IJMS 21 (2020) 8671, https://doi.org/10.3390/ijms21228671.
[46] Q. Wei, L. Ma, Biofilm matrix and its regulation in Pseudomonas aeruginosa, IJMS 14 (2013), 20983, https://doi.org/10.3390/ijms141020983. –21005.
[47] L. Ma, M. Conover, H. Lu, M.R. Parsek, K. Bayles, D.J. Wozniak, Assembly and development of the Pseudomonas aeruginosa biofilm matrix, PLoS Pathog. 5 (2009), e1000354, https://doi.org/10.1371/journal.ppat.1000354.
[48] E. Pericolini, B. Colombari, G. Ferretti, R. Iseppi, A. Ardizzoni, M. Girardis, A. Sala, S. Peppoloni, E. Blasi, Real-time monitoring of Pseudomonas aeruginosa biofilm formation on endotracheal tubes in vitro, BMC Microbiol. 18 (2018) 84, https://doi.org/10.1186/s12866-018-1224-6.
[49] D. Bajrami, S. Fischer, H. Barth, M.A. Sarquis, V.M. Ladero, M. Fernández, MariaC. Sportelli, N. Cioffi, C. Kranz, B. Mizaikoff, In situ monitoring of Lentilactobacillus parabuchneri biofilm formation via real-time infrared spectroscopy, Npj Biofilms Microbiomes 8 (2022) 92, https://doi.org/10.1038/s41522-022-00353-5.
[50] J. Masák, A. Čejková, O. Schreiberová, T. Řezanka, *Pseudomonas* biofilms: possibilities of their control, FEMS Microbiol. Ecol. 89 (2014) 1–14, https://doi.org/10.1111/1574-6941.12344.
[51] S. Galié, C. García-Gutiérrez, E.M. Miguélez, C.J. Villar, F. Lombó, Biofilms in the food industry: health aspects and control methods, Front. Microbiol. 9 (2018) 898, https://doi.org/10.3389/fmicb.2018.00898.
[52] W. Jun, M.S. Kim, B.-K. Cho, P.D. Millner, K. Chao, D.E. Chan, Microbial biofilm detection on food contact surfaces by macro-scale fluorescence imaging, J. Food Eng. 99 (2010) 314–322, https://doi.org/10.1016/j.jfoodeng.2010.03.005.
[53] B.K. Mortensen, Detection of Biofilms, Cracks, and Pores in Stainless Steel Tanks in the Food Industry, Bactoforce, 2014. https://bactoforce.com/wp-content/uploads/2021/10/Detection-of-biofilms-cracks-and-pinholes-Borge-Mortensen-2014-02-28.pdf.
[54] M. Tabacco, M. Mittelman, J. Schanzie, Real-time Biofilm Monitoring System, US20050151971A1, 2005. https://patents.google.com/patent/US20050151971/en. (Accessed 18 April 2023).
[55] E.E. Mann, D.J. Wozniak, *Pseudomonas* biofilm matrix composition and niche biology, FEMS Microbiol. Rev. 36 (2012) 893–916, https://doi.org/10.1111/j.1574-6976.2011.00322.x.
[56] E. Tacconelli, E. Carrara, A. Savoldi, S. Harbarth, M. Mendelson, D.L. Monnet, C. Pulcini, G. Kahlmeter, J. Kluytmans, Y. Carmeli, M. Ouellette, K. Outterson, J. Patel, M. Cavaleri, E.M. Cox, C.R. Houchens, M.L. Grayson, P. Hansen, N. Singh, U. Theuretzbacher, N. Magrini, A.O. Aboderin, S.S. Al-Abri, N. Awang Jalil, N. Benzonana, S. Bhattacharya, A.J. Brink, F.R. Burkert, O. Cars, G. Cornaglia, O. J. Dyar, A.W. Friedrich, A.C. Gales, S. Gandra, C.G. Giske, D.A. Goff, H. Goossens, T. Gottlieb, M. Guzman Blanco, W. Hryniewicz, D. Kattula, T. Jinks, S.S. Kanj, L. Kerr, M.-P. Kieny, Y.S. Kim, R.S. Kozlov, J. Labarca, R. Laxminarayan, K. Leder, L. Leibovici, G. Levy-Hara, J. Littman, S. Malhotra-Kumar, V. Manchanda, L. Moja, B. Ndoye, A. Pan, D.L. Paterson, M. Paul, H. Qiu, P. Ramon-Pardo, J. Rodríguez-Baño, M. Sanguinetti, S. Sengupta, M. Sharland, M. Si-Mehand, L.L. Silver, W. Song, M. Steinbakk, J. Thomsen, G.E. Thwaites, J.W. Van Der Meer, N. Van Kinh, S. Vega, M.V. Villegas, A. Wechsler-Fördös, H.F.L. Wertheim, E. Wesangula, N. Woodford, F.O. Yilmaz, A. Zorzet, Discovery, research, and development of new antibiotics: the WHO priority list of antibiotic-resistant bacteria and tuberculosis, Lancet Infect. Dis. 18 (2018) 318–327, https://doi.org/10.1016/S1473-3099(17)30753-3.
[57] R. Jia, D. Yang, D. Xu, T. Gu, Anaerobic corrosion of 304 stainless steel caused by the Pseudomonas aeruginosa biofilm, Front. Microbiol. 8 (2017) 2335, https://doi.org/10.3389/fmicb.2017.02335.
[58] C.U. Schwermer, D. De Beer, P. Stoodley, Nitrate respiration occurs throughout the depth of mucoid and non-mucoid Pseudomonas aeruginosa submerged agar colony biofilms including the oxic zone, Sci. Rep. 12 (2022) 8557, https://doi.org/10.1038/s41598-022-11957-4.
[59] E. Werner, F. Roe, A. Bugnicourt, M.J. Franklin, A. Heydorn, S. Molin, B. Pitts, P. S. Stewart, Stratified growth in *Pseudomonas aeruginosa* biofilms, Appl. Environ. Microbiol. 70 (2004) 6188–6196, https://doi.org/10.1128/AEM.70.10.6188-6196.2004.
[60] D. Fleming, W. Redman, G.S. Welch, N.V. Mdluli, C.N. Rouchon, K.L. Frank, K. P. Rumbaugh, Utilizing glycoside hydrolases to improve the quantitation and visualization of biofilm bacteria, Biofilms 2 (2020), 100037, https://doi.org/10.1016/j.bioflm.2020.100037.
[61] R. Hartley, A. Zisserman, Multiple View Geometry in Computer Vision, second ed., Cambridge University Press, Cambridge, UK ; New York, 2003.
[62] G. Bradski, The OpenCV library, Dr. Dobb's Journal of Software Tools (2000) 122–125.
[63] F. Pedregosa, R. Weiss, M. Brucher, Scikit-learn: Machine Learning in Python, 2011, pp. 2825–2830.
[64] A. Rinnan, F.V.D. Berg, S.B. Engelsen, Review of the most common pre-processing techniques for near-infrared spectra, TrAC, Trends Anal. Chem. 28 (2009) 1201–1222, https://doi.org/10.1016/j.trac.2009.07.007.
[65] D.P. Kingma, J. Ba, Adam: a Method for Stochastic Optimization, ICLR, 2015.